Desalination and Water Treatment
www.deswater.com

doi: 10.5004/dwt.2020.25768

192 (2020) 340–357
July

Hydroxyapatite conjugated graphene nanoplatelets vs. multi-walled carbon nanotubes for enhanced dye removal

Vijaykiran N. Narwade[a,b,*], Janez Kovac[c], Kashinath A. Bogle[a], Vanja Kokol[b,*]

[a]*School of Physical Sciences, Swami Ramanand Teerth Marathwada University, Nanded, MS 431606, India, Tel. +919765734431; email: vkiranphysics@gmail.com (V.N. Narwade), Tel. +917350845827; email: kashinath.bogle@gmail.com (K.A. Bogle)*
[b]*Faculty of Mechanical Engineering, University of Maribor, Smetanova ul.17, 2000 Maribor, Slovenia, Tel. +386-2-220-7896; Fax: +386-2-220-7990; email: vanja.kokol@um.si (V. Kokol)*
[c]*Department of Surface Engineering and Optoelectronics, Jozef Stefan Institute, Jamova 39, 1000 Ljubljana, Slovenia, Tel. +386-1-477 3403; email: janez.kovac@ijs.si (J. Kovac)*

Received 27 July 2019; Accepted 28 February 2020

ABSTRACT

The hydroxyapatite (HAp) was conjugated on carboxylated graphene nanoplatelets (Gra-C to GHAp) or multi-wall carbon nanotubes (CNT-C to CHAp) by its in-situ synthesis using the wet-chemical precipitation method, to increase their surface areas and, thus, negatively-charged active sites for adsorption of cationic pollutants as dyes from a water solution. Various characterization techniques have been utilised for the analysis of crystallinity, bulk and surface chemistry, as well as the morphological structure of synthesized nanocomposites, while Rhodamine 6G was used in adsorption experiments as target pollutant to study. The results show much higher adsorption capacity (90 mg g^{-1}) for GHAp, compared to CHAp (59 mg g^{-1}) or their original counterparts (6.5 mg g^{-1} for HAp, 25 mg g^{-1} for Gra-C, 20 mg g^{-1} CNT-C), be related to quantitatively higher electrostatic attraction of dye molecules with the surface located carboxylic and phosphorus groups from Gra-C and equally distributed HAp particles, respectively, resulting to a monolayer adsorption capacity and heterogeneous sorption. Pseudo-second-order kinetic and Freundlich isotherm model are revealed to be the best described their adsorption behavior. The reusability of nanocomposites was also confirmed by up to 77% of adsorption efficiency after three repeated desorption and regeneration cycles, indicating them as a promising adsorbent for dyes removal from wastewater.

Keywords: Graphene; Carbon nanotubes; Hydroxyapatite; Synthesis; Nanocomposites; Dye adsorption

1. Introduction

The estimated annual production of commercially available dyes is approximately 7×10^5 *t*, being used widely in the synthesis, printing, textile, pulp mill, food and cosmetic industries [1]. Most of the dyes are environmentally toxic, and some of their products have a mutagenic or carcinogenic influence on human beings [2,3]. Dye decolourization is, thus, still the most studied by using different methods, such as biological treatment [4,5], chemical oxidation [6,7], coagulation/flocculation [8,9], ion exchange [10,11], membrane separation [12,13] and adsorption [14–16]. However, except for the adsorption method, almost all of them have relatively high operating costs and a secondary sludge disposal problem.

Various adsorbents, such as rice husk [17,18], agricultural peel [19–21], cellulose [22,23], and activated carbon [24–26], have thus been studied for adsorption of dyes from aqueous solutions. Among them, carbon nanotubes (CNTs) and graphene nanoplatelets represent new

* Corresponding authors.

emerged carbonaceous nanomaterials, the characteristic molecular structures of which make them interact strongly with organic molecules via non-covalent forces (such as hydrogen bonding, π–π stacking, electrostatic and van der Waals forces), and hydrophobic interactions [27,28]. Their nanosized structures also endow them with rapid equilibrium rates, high adsorption capacity, and effectiveness over a broad pH range [29,30]. High adsorption capacity (270.27, 243.90, and 188.68 mg g^{-1}) of activated carbon (AC), graphene oxide (GO) [31] and CNTs [32–34] for methylene blue dye, respectively, were thus shown to be not only due to the large surface area of the particles but also due to π–π electron donor-acceptor interactions and electrostatic attraction of oppositely charged adsorbate − adsorbent species, which is governed by the pH and temperature of the medium [33–35]. Along with this, various graphene composites are studied for effective removal of dyes, like magnetic graphene [36,37], chitosan-GO [38] and magnetic cellulose/GO [39].

Calcium hydroxyapatite (HAp), $Ca_{10}(PO_4)_6(OH)_2$, is another low cost and highly stable inorganic material, whose structure, ion exchange capacity, adsorption affinity, and capacity to bond with organic molecules, have attracted much attention in the last decade [40]. The adsorption of heavy metals such as Pb^{2+}, Cu^{2+}, $Co^{2+}$and Cd^{2+} from aqueous solutions on HAp has been attributed to the ion exchange of Ca^{2+} on the HAp by the metal cation in the solution [41–43]. HAp and its nanocomposites, such as for example, HAp-GO [44] and Ag-doped HAp [45] were also studied as adsorbents for dyes from wastewater, yielding up to 554 mg g^{-1} capacity. Recently, graphene sheets were functionalised with HAp through chemical precipitation, without [24,26] or with dopamine pre-polymerization [25], followed optionally by plasma sintering [27], in order to increase their reactivity. *In-situ* chemical vapor deposition was also used to prepare CNT-HAp nanocomposites [24,25], however, with poor interfacial interactions between the CNTs and HAp, resulting in an unsatisfactory load transfer from the matrix to the CNTs [26].

In this study, differently structured and carboxylated graphene (Gra-C) nanoplatelets and multi-wall carbon nanotubes (MWCNT-C) were used for surface modification with HAp, being synthesized in-situ in the presence of nanomaterials by the wet precipitation method and using different molar concentrations of calcium nitrate and di-ammonium hydrogen phosphate as HAp precursors. The prepared nanocomposites were well characterised relating to the structure, crystallinity and surface properties (charge and morphology), before being used for investigation of cationic Rhodamine 6G.dye removals as a function of initial pH, dye concentration, dosage and contact time. The reason for the selection of Rhodamine 6G as target adsorbate because its exposure can cause several acute and chronic health hazards. The possible routes of exposure may be inhalation, ingestion, skin contact, eye contact. Hence may cause irritation to respiratory tract, toxic effects exerted upon nervous system particularly optic nerve, symptoms of overexposure may include headache, nausea, blurred vision, vomiting, blindness, coma and death. The kinetic and isotherms models are also used to evaluate the maximum adsorption capacities and rate of adsorptions.

2. Experimental

2.1. Materials

Di-ammonium hydrogen phosphate ($(NH_4)_2HPO_4$), calcium nitrate tetrahydrate ($Ca(NO_3)_24H_2O$), ammonia solution 25% (NH_4OH), hydrochloric acid (HCl), sodium hydroxide (NaOH), and Rhodamine 6G dye were purchased from Sigma-Aldrich chemicals (Germany). Carboxylated graphene nanoplatelets (20–30 nm, grade of 4.99%) and carboxylated multi-wall carbon nanotubes (20–30 nm, grade of 6.99%) were purchased from Cheap Tubes Inc., (USA). The chemicals were used as received. MilliQ water of 18.2 MΩ was used throughout the experiments.

2.2. Synthesis of hydroxyapatite (HAp)

HAp is synthesized by using the wet chemical precipitation method in which calcium nitrate tetrahydrate ($Ca(NO_3)4H_2O$) and di-ammonium hydrogen phosphate ($(NH_4)_2HPO_4$) were used as precursors. The molar concentrations of the above materials were maintained so as to have the ratio of Ca/P of 1.67 [46]. The precipitation procedure is carried out by dropwise addition of 0.6 M di-ammonium hydrogen phosphate into 1 M calcium nitrate tetrahydrate solution, under constant stirring of 150 rpm at 80°C for 4 h, followed by ageing for about 24 h. The white precipitates are then washed 3–4 times with MilliQ water to remove the rest of the precursors, and dried in an air oven at 100°C.

2.3. Synthesis of graphene and MWCNT based HAp nanocomposites

50 ml of 1 or 0.5 M calcium nitrate tetrahydrate solution is added dropwise to 0.01 g of carboxylated graphene (Gra-C) and MWCNT (CNT-C) suspensions, respectively. The solutions were stirred for nearly 30 min before 50 ml of 0.6 or 0.3 M di-ammonium hydrogen phosphate solution was added at 80°C and pH of 11, being adjusted with ammonia solution. The synthesis was carried out under constant stirring of 150 rpm at 80°C for 4 h, followed by ageing for about 24 h. Finally, the precipitates are filtered (Whatman filter paper no. 42), washed 3–4 times with MilliQ water to remove the excess of precursors and ammonia, and dried in an air oven at 100°C. The experimental parameters are listed in Table 1, while the formation of composites is shown in Fig. 1a.

2.4. Characterization

The crystalline structure of the samples is evaluated by X-Ray Diffraction (XRD) analysis using a Rigaku MiniFlex2 (Germany) diffractometer with a scanning rate of 2°/min and a Cu Kα radiation source (λ = 1.54 Å) operating at 40 kV and 30 mA for a range of diffraction angles (2θ) between 5°–60°. The crystallite size of HAp at the (002) plane [46] is calculated by Scherer's equation, and the interplanar distance (d_{hkl}) as a function of $a = b$ and c for a hexagonal lattice:

$$D = \frac{k\lambda}{\beta\cos\theta} \quad (1)$$

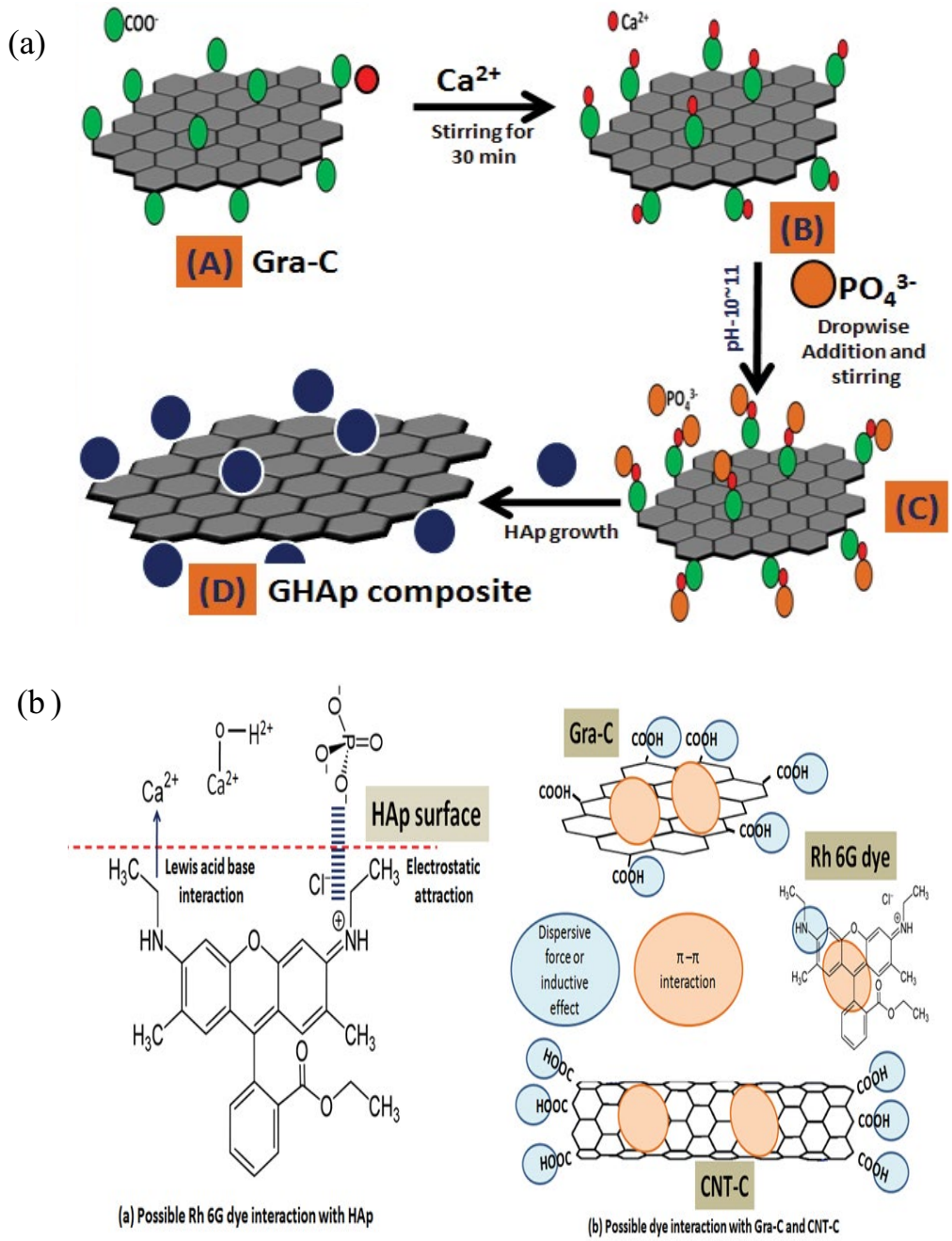

Fig. 1. Proposed mechanism (a) for *in-situ* synthesis of GHAp nanocomposite by the wet chemical precipitation method and (b) possible interactions of Rh 6G dye molecule with HAp, Gra-C and CNT-C.

$$\frac{1}{d_{hkl}^2} = \frac{4}{3} \times \frac{\left(h^2 + hk + k^2\right)}{a^2} + \frac{1}{c^2} \tag{2}$$

where D is the average crystallite size, β is the full width of the peak at half of the maximum intensity (rad), λ is the wavelength of X-ray radiation (1.54 Å), and k is a constant related to the crystallite size of the HAp.

Fourier transform infrared (FTIR) spectroscopy is recorded to identify the functional groups and surface chemistry of the adsorbents using a Perkin-Elmer spectrum one FTIR spectrometer (UK) with a Golden Gate ATR attachment and a diamond crystal. The spectra were carried out at ambient conditions from accumulating 16 scans at a 4 cm^{-1} resolution over a region of 4,000–650 cm^{-1}, and with air spectrum subtraction performed in parallel as a background. The Spectrum 5.0.2 software programme was applied for the data analysis. All the measurements are carried out in duplicate.

The structure and morphology of the adsorbents were characterised by using a low-vacuum scanning electron

Table 1
Experimental parameters used for the GHAp/CHAp nanocomposite synthesis

Sample	Molarity of $Ca(NO_3)_4H_2O$ (M)	Amount in grams (g)	Molarity of $(NH_4)_2{\cdot}HPO_4$ (M)	Amount in grams (g)	Amount of Gra-C vs. CNT-C (g)
GHAp 1	1	11.807	0.6	3.450	0.01 Gra-C
GHAp 0.5	0.5	5.9035	0.3	1.7253	0.01 Gra-C
CHAp 1	1	11.807	0.6	3.450	0.01 CNT-C
CHAp 0.5	0.5	5.9035	0.3	1.7253	0.01 CNT-C

microscopy (SEM) (FEI Quanta 200 3D, Thermo Fisher, USA). The pieces of dried samples were sputter-coated with gold before being examined up to three times using back-scattered modes and secondary electron (SE) modes at different magnifications up to 1,00,000 times. A high-vacuum field-emission SEM FEI Sirion NC 400 with back-scattered electron detector was used within a magnification range of 250–2,00,000 times.

A Malvern Zetasizer Nano-ZS instrument and disposable DTS 1060C zeta-potential cells (Malvern Instruments Ltd., Malvern, UK) were used for determining the zeta-potential of the adsorbent particles in a water suspension of 0.05% (w/w) at a temperature of 20°C ± 0.2°C. An applied voltage of 50 V was used. The zeta potential was determined at pH from 3 to 11 by adjusting the pH of the solution with 0.1 M HCl and 0.1 M NaOH, respectively. An average of three measurements was calculated.

The X-ray photoelectron spectroscopy (XPS or ESCA) analyses were carried out on the PHI-TFA XPS spectrometer manufactured by Physical Electronics Inc., (USA). Samples were mounted on a metallic sample holder and introduced in the ultra-high vacuum spectrometer in the range of 10^{-9} mbar. The analysed area was 0.4 mm in diameter, and the analysed depth was about 3–5 nm. Sample surfaces were excited by X-ray radiation from a monochromatic Al source at a photon energy of 1,486.6 eV. The survey wide-energy spectra were taken over an energy range of 0–12,400 eV with a pass energy of the analyser of 187 eV in order to identify and quantify elements present on the surface. The high-energy resolution spectra were acquired with the energy analyser operating at a resolution of about 0.6 eV and pass energy of 29 eV. The accuracy of binding energies was about ±0.3 eV. Quantification of surface composition was performed from XPS peak intensities, taking into account the relative sensitivity factors provided by the instrument manufacturer. Two-three measurements were performed on each sample and the average composition was calculated. The relative error in composition was estimated to be about 20% of the reported concentration. It originates from not well-known relative sensitivity data and from the heterogeneous surface composition. Although during XPS analyses a low energy electron beam was used for charge compensation, there was a shift of a few eV of XPS spectra due to charging of the HAp treated materials. Therefore, the spectra were calibrated on the energy scale, setting the Ca $2p_{3/2}$ peak at 247.2 eV, characteristic for a HAp compound.

2.5. Rhodamine 6G dye adsorption study

Adsorption experiments were carried out in batches using 0.1 g L^{-1} as a stock solution, prepared by dissolving Rhodamine 6G in deionised water. Experiments are carried out in 100 mL Erlenmeyer flasks containing 40 mL of Rhodamine 6G solution of different concentrations (5, 10, 20, 30, 50, and 75 mg L^{-1}) and the same amount (0.01 g) of sorbents, at 150 rpm using a rotary shaker. The initial pH of the solution was adjusted to 9.0 by adding small amounts of 0.1 M NaOH solution. The concentration of Rhodamine 6G in a solution, before and after adsorption, is determined at different time periods by optical absorption evaluated at 526 nm using a plate reader equipped with a Tecan UV-Vis spectrophotometer. The average values, as well as the standard deviation of the mean values, were calculated from at least four individual measurements. The removal of Rhodamine 6G in the percentage, and as a per unit of sorbent dry weight, is calculated by the following equations [46,47]:

$$q_e = \frac{V}{M}\left(C_0 - C_i\right) \tag{3}$$

$$\%\ \text{Removal} = \frac{\left(C_0 - C_i\right)}{C_0} \times 100 \tag{4}$$

where q_e is the maximum adsorption limit at equilibrium (mg g^{-1}), V is the volume of dye solution (L), C_0 is the initial dye concentration in a solution (mg L^{-1}), C_i is the final concentration of dye in a solution (mg L^{-1}), and M is the weight of adsorbent (g). The adsorbent dosage (0.25–2 g L^{-1}) and solution pH (2–9) were studied along with the above-mentioned initial concentration parameter.

For desorption, the dye adsorbed adsorbents were dispersed in a methanol solution containing 4% acetic acid. After desorption, the clear supernatant solution was collected and the percentage of dye desorption (De%) was calculated using the following equation [47]:

$$\text{De}(\%) = \frac{\text{Dye desorbed}\left(\text{mg L}^{-1}\right)}{\text{Dye adsorbed}\left(\text{mg L}^{-1}\right)} \times 100 \tag{5}$$

The results of adsorptions were evaluated by the root mean sum-of-squares error equation (RMSE) [48]:

$$\text{RMSE} = \sqrt{\frac{1}{n}\sum_{i=1}^{n}\left(q_{\text{exp}} - q_{\text{cal}}\right)^2} \tag{6}$$

where q_{cal} is a kinetic model predicting the adsorption capacity value, q_{exp} is the experimental adsorption capacity value, and n is the number of points.

3. Results and discussion

3.1. Characterization of nanocomposites

The proposed mechanism of HAp formation on carboxylated Gra-C nanoplatelets is presented in Scheme 1A. Gra-C have negatively charged carboxylic (–COOH) groups at their edges which work as anchor sites and, thus, strongly attracts Ca^{2+} ions from $Ca(NO_3)_4H_2O$ through electrostatic attraction and further phosphate ions (PO_4^{3-}) from $(NH_4)_2HPO_4$, thus nucleating the HAp on the surface of the Gra-C. As Gra-C have two basal planes, HAp will form between the staking of graphene layers [44]. Contrarily, by using carboxylated MWCNT (CNT-C), HAp formation will take place only on the surface of the CNT-C via available carboxylic groups which work as nucleating sites for HAp formation by the same mechanism.

Different analytical methods are used to characterise the structure and morphology of the nanocomposites synthesized.

The crystal structure and phase purity of Gra-C, CNT-C, HAp and its composites were characterised by the XRD diffractograms depicted in Fig. 2. The Gra-C shows its characteristic high-intensity peak at around 26.56° of 2θ, corresponding to the (002) plane of the graphene's highly crystalline structure [48]. On the other hand, the CNT-C shows two broad peaks centred at around 25.92° and 42.94°, being related to the (002) and (001) planes of carbon [49]. Synthesized HAp shows an exact resemblance in peak positions of the planes, except for peak broadness when compared to the commercial HAp, which is an indication of the relatively lower crystalline structure; the peaks are located at 2θ values of 25.96°, 32.09°, 32.76°, 34.09°, 39.90°, 46.71°, and 49.36°, corresponding to the related crystal planes at (002), (211), (112), (300), (202), (130), (222), and (213), respectively (JCPDS card no. 09–0432) [42,47]. The HAp modified CNT-C and Gra-C (i.e. CHAp and GHAp nanocomposites) showed the characteristic peaks of the synthesized HAp planes, with a significant presence of both Gra-C and CNT-C, respectively, being seen by an additional small peak at 26.25° in the case of GHAp composites, and a sharp peak at 25.9° in the case of the CHAp composite, overlapping with the (002) plane of the HAp. It can be also noted that other peaks of the composites (for GHAp at about 25.96°, 26.25°, 31.93°, 32.76°, 34.15°, 39.93°, 46.71°, and 49.53°, and for CHAp at about 25.84°, 32.01°, 32.93°, 34.09°, 39.57°, 46.71°, and 49.72), correspond to the crystal index planes (002), (211), (112), (300), (202), (130), (222) and (213) of the HAp. The relative sharpness of these peaks, being expressed a bit better in the case of GHAp, is an indication of the relatively good crystalline structure of HAp formed onto the Gra-C and CNT-C particle surfaces. However, the crystallite sizes of synthesized HAp (Table in Fig. 2), calculated from the peak at around 26°, corresponding to the indices at (002) of the HAp crystal index, is calculated to be higher

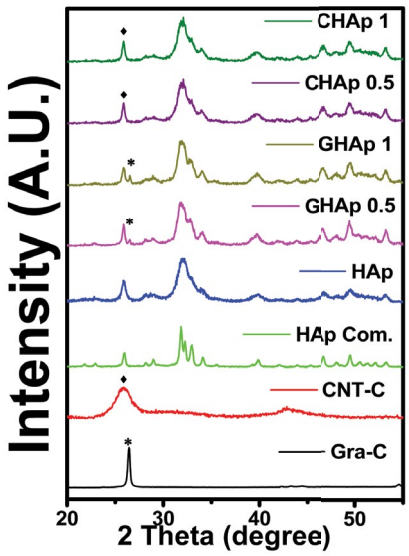

Adsorbent	HAp	GHAp 0.5	GHAp 1	CHAp 0.5	CHAp 1
Crystallite size of HAp (nm)	9.16	11.20	12.70	14.2	10.26
Crystal structure of HAp	Hexagonal crystal structure				
Lattice constants (nm)	a=b=0.94 c=0.68	a=b=0.94 c=0.68	a=b=0.94 c=0.68	a=b=0.94 c=0.68	a=b=0.92 c=0.68

Fig. 2. XRD diffractograms of HAp (synthesized and commercial), Gra-C, CNT-C, and their nanocomposites with the crystallite size and crystal structure of synthesized HAp.

(10.26 and 14.2 nm) for CHAp compared to GHAp (11.20 and 12.70 nm), and to that of pure synthesized HAp (9.16 nm), also dependent on the quantity of precursors used (0.5 and 1 M). The lattice constants were also calculated using the crystal lattice formula for hexagonal systems and the values obtained for the composites were similar to the HAp lattice constant parameters of $a = b = 0.94$ nm and $c = 0.68$ nm [46], except for the CHAp1 sample having $a = b$ of 0.92 nm.

The FTIR spectra of HAp and its composites are performed to get better insight about their chemical composition. As shown in Fig. 3, the FTIR spectrum of synthesized HAp is nearly identical to those obtained in the literature. The strong and sharp peaks appeared at about 1,022.98 cm^{-1}, as well as at about 602.33 and 561.33 cm^{-1}, corresponding to the stretching and bending modes of the P–O bond vibration of phosphate groups (PO_4^{3-}), respectively, of the HAp [50]. In addition, small and broader peaks at about 2,359.21; 1,422.15; and 1,022.98 cm^{-1} are seen, corresponding to the O=C=O stretching mode of CO_2, the stretching mode of $(CO_3)^2$, and *B*-type of CO_3^{2-} - $v3$ vibration mode, respectively [51–53]. All of these HAp characteristic peaks can be observed in the case of both nanocomposites with some small differences. The CHAp shows similar peaks with a small shifting of the peak at about 961 to 963 cm^{-1} that may be related to an increase of P–O bonds, coinciding with an increase of the crystallite size of HAp (Fig. 2, XRD data), as well as a very weak peak at around 1,300–1,400 cm^{-1} which may be the C–O stretch of the carboxylic groups. In the case of GHAp, an additional weak band is observed at around 875 cm^{-1} which is related to the CO_3^{2-} type *B*-$v2$ vibration mode and $v2$ vibration mode of HPO_4^{2-}, as well as two weak peaks at about 1,300 and 1,400 cm^{-1}, corresponding to the C–O stretching and O–H bending vibrations of anionized carboxylic groups, respectively.

The zeta potential values of samples as a function of pH were determined to get additional information on the adsorbents` surface charge being related to the ionization of different functional groups [46]. As seen from Fig. 4, the original and composites have a slightly positive or neutral surface charge at pH 3, which are becoming more negative by raising the pH to 11, however with a different slope. It can also be observed that the zeta potential values of original Gra-C are decreasing the most significantly, reaching a value of about –53.7 mV at pH 11 compared to the CNT-C reaching a zeta potential of –29.9 mV at pH 11. This indicates that plane Gra-C samples contain more and better available surface- and end-located anionic carboxylic reactive groups (Scheme 1A) which are ionized by an increase of pH from around 3.5 (as related to their pK value), compared to tubular CNT-C, having negative functional groups much less accessible. On the contrary, all the HAp composites show a similar trend of the slope decreases, similar to the pure HAp ones, indicating that both the Gra-C and CNT-C are surface modified with the HAp, however, with some small differences. A bit less-negative zeta potential values of both GHAp (–17.4 to –14.5 mV) composites at around the pH 9, compared to CHAp (–18.5 to –17.0 mV) may be the consequence of a differently structured HAp on the Gra-C vs. CNT-C surfaces with newly introduced phosphoric acid groups of pKas at about pH 2, 7, and 12, besides the remaining carboxylic groups also contributing to the different ionization effect.

The surface chemistry of the samples was also investigated employing the XPS technique. In Fig. 5a, the wide energy scale XPS spectrum of the sample GHAp 0.5 is shown, being also typical for all analysed nanocomposites. The spectrum contains C 1s, O 1s, P 2p, P 2s, Ca 2p, Ca 2s and O 2s peaks, revealing the presence of Ca, P, O and C elements. By using the intensities of C 1s, O 1s, Ca 2p and Ca 2p peaks in the XPS spectra, chemical composition was calculated in the surface region of a thickness of about 5 nm (Fig. 5, inserted Table). The Ca/P ratio, being calculated from the ratio of concentration for Ca and P, is not stoichiometric (1.67), stable HAP phases have been found to exist over a range of Ca/P ratios from 1.2 to 1.5, correspond to the precursor concentration (0.5 to 1 M), indicating that more phosphorus-based groups are bounded from the higher molar solution. For charge compensation, the XPS spectra were calibrated on the energy scale, setting the Ca 2p3/2 peak at 247.2 eV characteristic for a HAp compound. On the other hand, the spectra of P 2p were at 133.2 eV and the spectra of O 1s at 531.3 eV, being related to PO_4^{3-} species [54]. All of these binding energies are characteristic for a HAp compound, confirming the formation of HAp on both the graphene and CNT surfaces. At the same time, the carbon concentration obtained from the XPS spectra on the surface is in the range 10–25 at.%, and it originates partially from the graphene and CNT material incorporated in the nanocomposites, and partially from surface contamination, which is always present on air-exposed samples. The carbon C 1s spectra from the nanocomposites are rather broad (FWHM ~ 3–4 eV), showing either possible differential charging on the microscopic level due to the dielectric nature of HAp or different types of carbon bonds (Fig. 5b). This charging is frequently observed in the photoelectron spectra from materials with low electrical conductivity such as ceramics [55]. As may be seen from Fig. 5b, the C 1s spectra are dominated by a strong peak at 284.8 eV, corresponding to the non-oxygenated C–C ring (C1). At higher binding energies the contributions of C–O/C–OH/C–O–C (hydroxyl and epoxide, C2), O–C–O/C=O (carbonyl, C3), and O–C=O (carboxyl, C4) bonds at 286.5, 288.0, and 289.5 eV, respectively, can be also detected. An absolute presence of hydroxyl and epoxide groups at GHAp compared to CHAp samples with comparable carbonyl and higher carboxyl groups content, can be observed, evidencing on a generally higher oxygen degree in CHAp determined by the oxygenated functional groups located on its surface. On the other hand, a reduction of peak intensities for same of these groups at GHAp with the increasing of precursors concentration (from 0.5 to 1 M), reveal on differently structured HAp on it surface. These observations are in agreement with results from FTIR and zeta-potential studies, provides a base for the understanding of the growth of HAp.

The surface morphology of synthesized HAp and its nanocomposites was examined by SEM imaging as depicted in Fig. 6. The nanocomposites prepared with higher HAp precursor content (GHAp 1 and CHAp 1) are more dense compared to ones prepared with a lower amount of HAp precursors (CHAp 0.5 and GHAp 0.5), having also more uniformly distributed particles of differently large aggregates, being more expressed in the case of the CHAp 1 sample. By using lower HAp precursor concentrations, the distribution of synthesized nanoparticles is much more irregular,

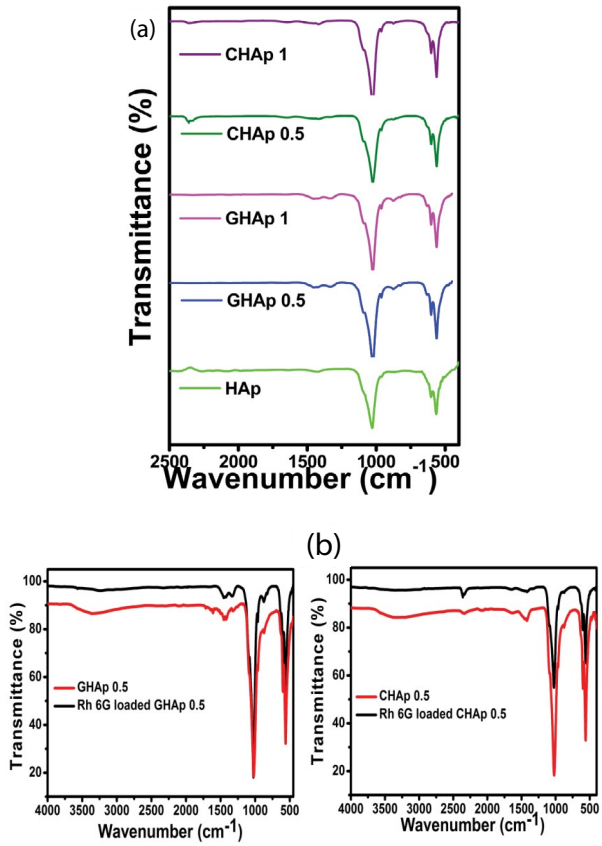

Adsorbent	HAp	GHAp 0.5	GHAp 1	CHAp 0.5	CHAp 1
O=C=O stretching mode of CO_2	2,359.21	2,358.70	2,358.93	2,359.34	2,358.63
Stretching mode of the $(CO_3)^2$	1,422.15	1,420.17	1,454.94	1,418.72	1,418.64
B-type CO_3^{2-}–v3 vibration mode	1,022.98	1,022.04	1,022.04	1,022.04	1,022.24
Symmetric stretching modes of the P–O bonds	961.33	961.90	962.43	963.10	963.30
CO_3^{2-} type B- v2 vibration mode; v2/HPO_4^{2-}	–	875.61	875.13	–	–
O–P–O bond vibrations	602.33 561.33	600.81 561.05	600.49 561.05	601.04, 561.24	600.95 561.85

Fig. 3. FTIR spectra of (a) HAp and HAp-based nanocomposites and (b) selected GHAp and CHAp nanocomposites before and after Rh 6G dye adsorption.

being the more expressed in case of the CHAp 0.5 samples. It is clear that the presence of Gra-C or CNT-C induces the heterogeneous nucleation of Hap, and further modulates the kinetics and morphology of HAp crystal growth, depending on the type of the available surface morphology (plane Gra-C vs. tubular CNT-C) and quantity of available functional carboxylic groups acting as a binding site to form HAp nuclei. The particle size is, namely, associated with the nucleation and growth of the pattern, which is also related highly to the degradation of supersaturation in the liquid phase as has been presented in Scheme 1A. The Gra-C, having a much higher amount of available negative functional groups acting as cavities formed in between the stacking of the graphene layer, permits fast and easy interactions with HAp precursors (Ca^{2+} ions binding through ion-dipolar forces followed by PO_4^{3-} ions binding through coordination interactions)

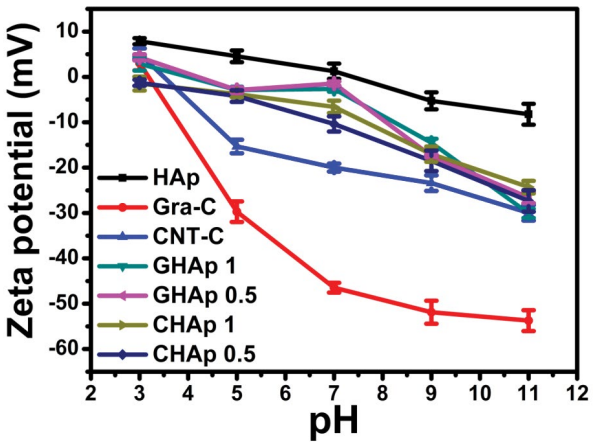

Fig. 4. Zeta potential plots of HAp, Gra-C, CNT-C, and differently synthesized HAp-based nanocomposites.

onto its surface, as well as into its inner layers of graphene [44], compared to the CNT-C that provides the active sites for Ca^{2+} binding only on its surface. Consequently, the physical growth of HAp could be identified as more homogenous and smaller in particle size for hybrids synthesized in the presence of Gra-C, compared to bigger particles in the case of using CNT-C with low efficient nucleation sites.

The inserted EDS data show the reduction of O and increase of C for both nanocomposites synthesized with higher HAp precursors' concentration compared with their counterparts. All samples also contain Ca and P, which Ca/P ratio is greater than the 1.67 of the used precursors, indicating synthesis of a Ca^{2+} rich apatite structure. However, this is most apparent in the case of HAp (Ca/P of 2.14) compared to other synthesized nanocomposites.

3.2. Adsorption studies

3.2.1. Effect of solution pH

Different solution pH values were used to investigate the effect of pH on the adsorption of Rhodamine 6G (Rh 6G) on the nanocomposites, and the obtained results are depicted in Fig. 7a. The Hap, as well as the nanocomposites, shows an increase in % removal of the dye as the solution pH increases, being the highest at pH 9. However, while the removal is around 16.89% for HAp, it is increased from about 50.55% and 42.70% at Gra-C and CNT-C to about 87.12% and 82.18% for GHAp *vs.* 75.55% and 72.24% for CHAp, being prepared by 1 and 0.5 M of HAp precursors, respectively.

Such an increase of cationic Rh 6G adsorption on the GHAp and CHAp could be explained by quantitatively higher sites of negatively-charged groups arising from available carboxylic groups of Gra-C and CNT-C and additional phosphorus groups from HAp conjugated on their surfaces, both interacting electrostatically with the positively charged dye at pH 9, as depicted schematically in Scheme 1B. On the contrary, in the acidic medium, the positively charged surface sites on the HAp and Rh 6G cations are submitted to electrostatic repulsions which, besides the H^+ competition, do not favor the adsorption of the dye. However, a considerable amount of Rh 6G was absorbed by HAp at lower pH values, which suggested that other mechanisms might also be involved in the Rh 6G adsorption process. It was reported that a strong H-bonding interaction between the P–OH group of HAp and the nitrogen atom of the Rh 6G molecule [31], as well as Lewis acid-base interaction with the Ca^{2+} groups of HAp [56], could contribute toward its adsorption. In both nanocomposites, the π–π electron donor-acceptor interaction (coupling) between C=C double bonds of Rh 6G benzene rings and Gra-C vs. CNT-C surface may also be involved, being more in favor at Gra-C with a larger and smoother surface, compared to tubular CNT-C, which makes Gra-C as the higher adsorption capability. As shown in Fig. 3, the characteristic peaks of FTIR spectra for GHAp and CHAp adsorbents, before and after Rh 6G dye adsorption, are similar, with small changes in red shifting and decrease in absorbance peak intensities at around 1,022.98, 602.45; and 561.33 cm^{-1}, corresponding to the stretching and bending modes of the P–O bond vibration of the phosphate groups (PO_4^{3-}), which indicates these groups interaction with the dye molecules.

3.2.2. Effect of adsorbent dosage

The effects of nanocomposites dose (0.1–0.9 g L^{-1}) on Rh 6G adsorption (Fig. 7b) increases for all composites until a dosage of around 0.5 g L^{-1}, when the active sites on the adsorbent surface available for adsorption are becoming saturated. The adsorption of dye molecules is, however, reducing from 86.89% and 82.09% to75.54% and 72.08% for GHAp and CHAp composites prepared with 0.5 and 1 g L^{-1} of HAp precursors, respectively. At the same time, the dye adsorption by synthesized HAp, Gra-C, CNT-C are reaching 15.98%, 55.88%, and 43.65%, respectively.

3.2.3. Effect of contact time – kinetic of adsorption

The adsorption of Rh 6G dye on the HAp, Gra-C, CNT-C and its composites was investigated as a function of contact time to determine the suitable time at which the adsorption process reaches equilibrium. Solutions of different initial dye concentrations were used with fixed amounts of adsorbent dose. As seen from Fig. 8, the initial adsorbent rate in the case of HAp is very slow, reaching equilibrium at about 50 min, with 24.54%, 24.62%, and 14.22% of removal and adsorption capacities of 2.54, 4.32, and 5.69 mg g^{-1} for dye concentration of 5, 10, and 20 mg L^{-1}, respectively. Gra-C and CNT-C reaches the equilibrium for all dye concentrations at nearly the same contact time (55–60 min), with the removal of 81.79% (8.17 mg g^{-1}) and 75.62% (7.65 mg g^{-1}) for dye conc. of 5 mg L^{-1}, 69.21% (13.84 mg g^{-1}) and 63.35% (12.67 mg g^{-1}) for dye conc. of 10 mg L^{-1}, and 50.55% (20.22 mg g^{-1}) and 45.70% (18.28 mg g^{-1}) for a dye conc. of 20 mg L^{-1}. Among all HAp-conjugated nanocomposites, the GHAp 0.5 shows the highest removal efficacy, that is, 94.88% (9.48 mg g^{-1}) and 86.99% (34.79 mg g^{-1}) for 5 and 20 mg L^{-1} dye concentration, respectively, and reaches equilibrium at nearly 60 min; this maybe due to the formation of much lower particle size using 0.5 g L^{-1} of HAp precursors (SEM, Fig. 7) and, thus, a higher amount of active sites on the GHAp surface (lower zeta-potential, Fig. 4) available for adsorption. Other

(a)

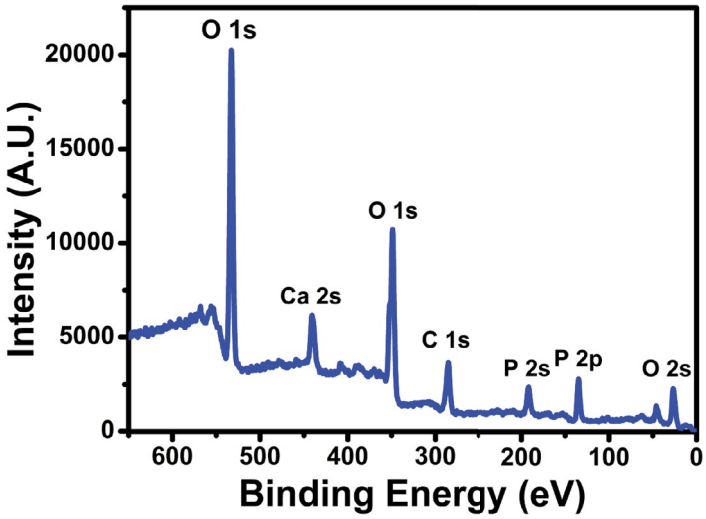

Elements (wt.%)	HAp Synthesised	GHAp 0.5	GHAp 1	CHAp 0.5	CHAp 1
C	9.6 ± 3	21.8 ± 4	12.4 ± 3	26.2 ± 5	23.7 ± 5
O	58.6 ±12	50.7 ± 11	56.7 ± 11	49.4 ± 10	49.6 ± 10
P	11.9 ± 3	10.1 ± 2	13 ± 3	9.8 ± 2	10.7 ± 2
Ca	17.4 ± 3	13.9 ± 3	16.1 ± 3	14.6 ± 3	13.6 ± 3
Ca/P ratio	1.46 ± 0.1	1.37 ± 0.1	1.23 ± 0.1	1.48 ± 0.1	1.27 ± 0.1

(b)

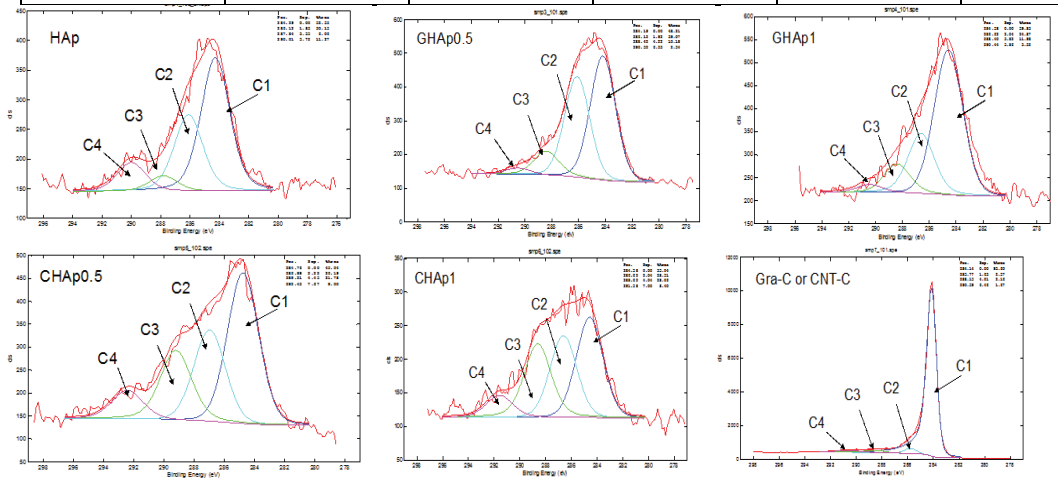

Fig. 5. XPS spectrum of (a) GHAp 0.5 nanocomposite sample with a surface composition of corresponding HAp and nanocomposites (inserted Table) and (b) high-resolution C1s spectra of differently prepared samples.

adsorbents (GHAp 1, CHAp 0.5 and CHAp 1) have the removal rates of 89.93% (8.99 mg g^{-1}), 89.91% (8.99 mg g^{-1}), and 88.03% (8.80 mg g^{-1}), respectively.

In order to explanation the mechanism and kinetics of rate-controlling steps during the adsorption of Rh 6G dye on synthesized nanocomposites, various kinetic models were used by using the experimental data whose results are presented in Fig. 9 and collected in Table 2.

The linear form of the pseudo-first-order kinetic model is given as [46]:

$$\frac{1}{q_t} = \frac{k_1}{q_1}\frac{1}{t} + \frac{1}{q_1} \tag{7}$$

where q_1 and q_t are the amounts of adsorbate molecules at equilibrium (mg g^{-1}) and at various time t, respectively, and k_1 is the rate constant (min^{-1}) of the first-order model for the adsorption process. Values of q_1 and k_1 are calculated from the plots of $1/q_t$ against $1/t$ (Figs. 9a and b). The maximum adsorption capacities are decreasing from 35.21, 34.84, 28.57,

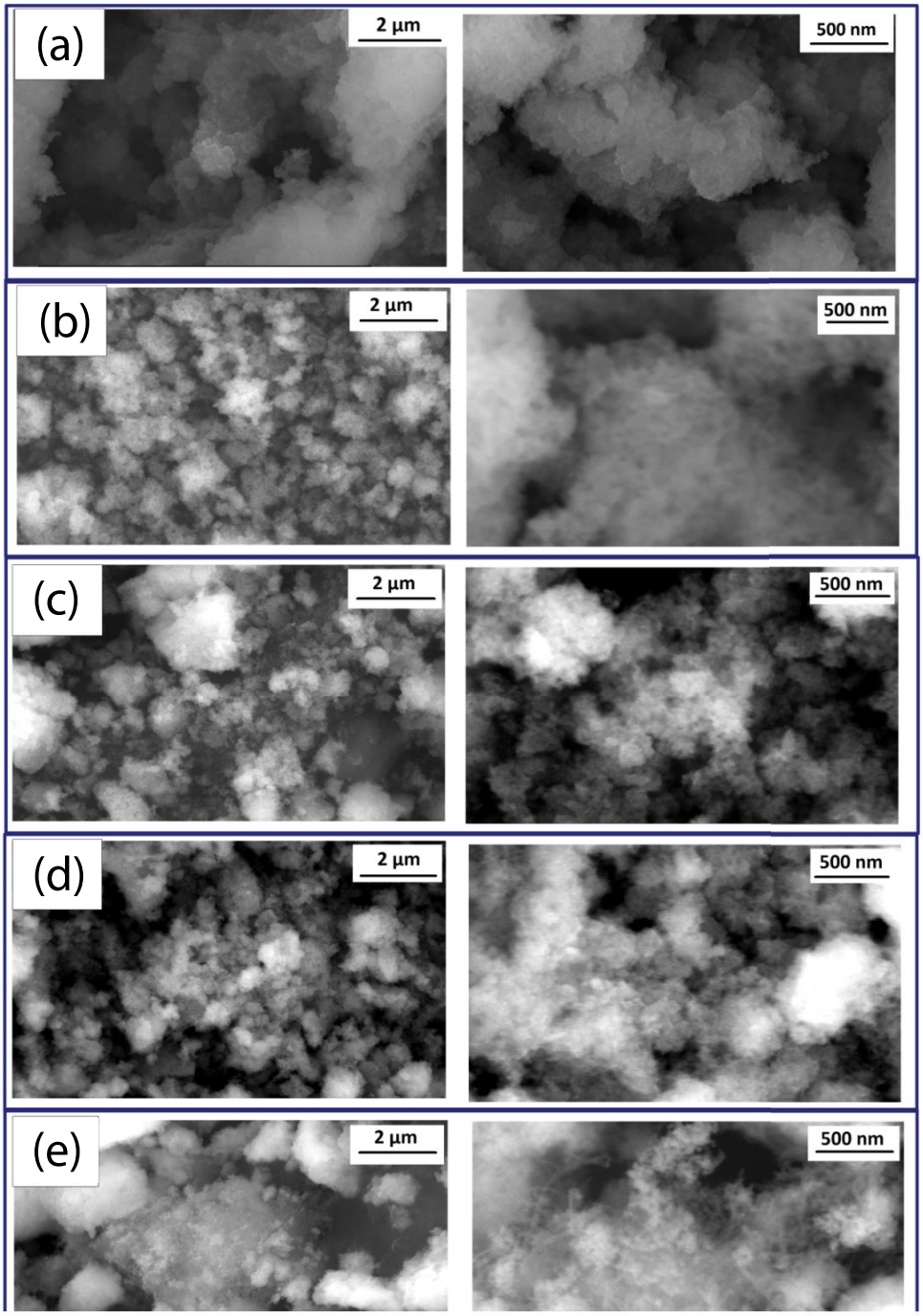

Elements (wt%)	HAp Synthesi sed	GHAp 0.5	GHAp 1	CHAp 0.5	CHAp 1
C	30.61 ± 2.28	39.91 ± 4.63	50.24 ± 1.35	24.74 ± 12.1	46.51 ± 2.28
O	40.27 ± 4.25	40.63 ± 1.82	32.88 ± 3.10	47.87 ± 5.31	40.24 ± 1.69
P	9.27 ± 0.63	7.06 ± 1.21	5.69 ± 0.65	9.19 ± 2.23	4.49 ± 0.32
Ca	19.85 ± 2.12	12.40 ± 1.85	11.19 ± 1.62	18.19 ± 4.84	8.77 ± 0.35
Ca/P ratio	2.14	1.75	1.96	1.97	1.95

Fig. 6. SEM images of (a) HAp, (b) GHAp 1, (c) GHAp 0.5, (d) CHAp 1, and (e) CHAp 0.5 with corresponding EDS analysis.

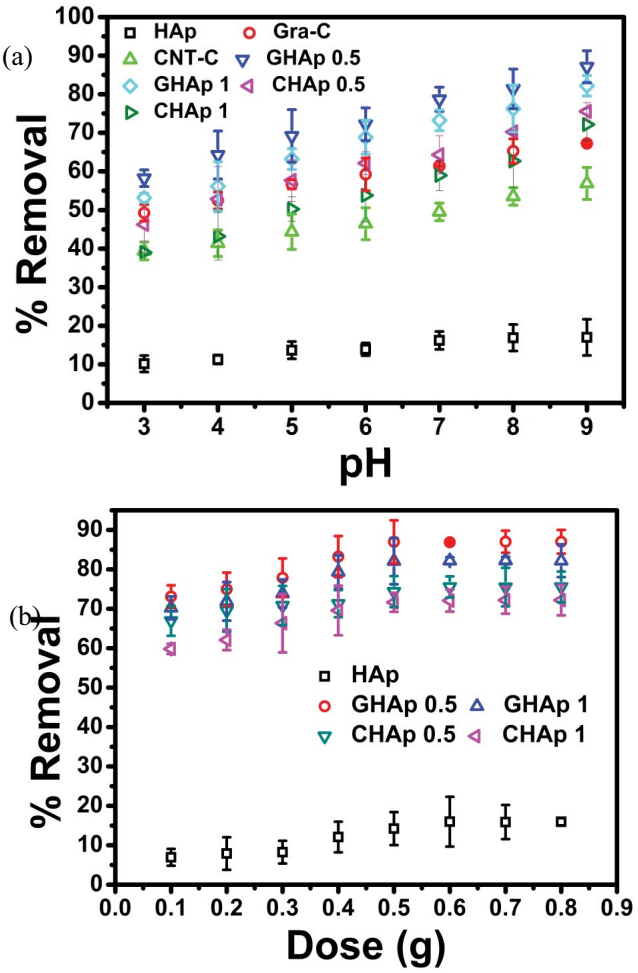

Fig. 7. Effect of (a) pH (using adsorbent dose of 0.5 g L^{-1}) and (b) adsorbent dosage on the removal of 20 mg L^{-1} Rh 6G dye with HAp and its nanocomposites after 300 min.

and 26.64 mg g^{-1} with RMSE values of 0.17, 0.82, 0.47, and 0.044, obtained for GHAp 0.5, GHAp 1, CHAp 0.5 and for CHAp 1, respectively, however with the R^2 values not fitted the best with this model above all those obtained for Gra-C and CNT-C used as adsorbents.

The linear form of the pseudo-second-order kinetic model is expressed as [42]:

$$\frac{t}{q_t} = \frac{1}{k_2 q_2^2} + \frac{t}{q_2} \tag{8}$$

where q_2 is the maximum adsorption capacity (mg g^{-1}) for the pseudo-second-order adsorption, q_t is the amount of dye adsorbed at equilibrium (mg g^{-1}) at time t (min), and k_2 is the rate constant of the pseudo-second-order adsorption (g mg^{-1} min^{-1}). Values of k_2 and q_2 are calculated from the plot of t/q_t vs. t (Figs. 9c and d). The calculated q_2 values of Rh 6G adsorption on composites (Table 2) were closer to the experimental values, with lower RMSE and high correlation coefficient (R^2 = 0.99). Calculated q_2 values for composites (with corresponding experimental values in brackets) are decreasing from 35.11 mg g^{-1} (34.79 mg g^{-1}), 34.24 mg g^{-1} (32.83 mg g^{-1}), 28.90 mg g^{-1} (29.74 mg g^{-1}) to 27.93 mg g^{-1} (26.65 mg g^{-1}) for GHAp 0.5, GHAp 1, CHAp 0.5 and CHAp 1, respectively. At the same time, the q_2 for HAp, Gra-C and CNT-C are 6.47, 23.80, and 19.84 mg g^{-1}, respectively.

The sorption kinetics may, alternatively, be also described. The overall adsorption process is controlled by either one or a combination of more steps, for example, film or external diffusion, pore diffusion, surface diffusion and adsorption on the pore surface. However, in a rapidly stirred batch, the diffusive mass transfer can be related by an apparent diffusion coefficient which will fit the experimental sorption rate data. Generally, a process is diffusion-controlled if its rate depends on the rate at which components diffuse towards one to another.

The transport of dye molecule from the aqueous solution to the surface of the composite adsorbents is thus followed by diffusion of the molecules into the interior pores of the adsorbent, which is likely to be a slow process and is, therefore, considered as a rate-determined step [57]. The Weber and Morris intraparticle diffusion model is used widely to analyze the nature of the rate-controlling step, which is represented by Eq. (9) to explain its mechanism [58]:

$$q_t = K_p t^{1/2} + I \tag{9}$$

where K_p is the intra-particle diffusion constant (mg g^{-1} $min^{-0.5}$) and I (mg g^{-1}) is the intercept. If the so–called Weber–Morris plot of q_t vs. $t^{1/2}$ gives a straight line, then the sorption process is controlled by the intra-particle diffusion process only. However, if the data exhibit multi-linear plots, then two or more steps influence the sorption process. In the case of Gra-C and CNT-C the plot of the intra-particle diffusion model (Figs. 9e and d) is nearly straight, indicating the diffusion stage is not occurring, and most of the dye molecules rapidly take places on a surface. On the other hand, two phases are observed in the case of HAp and all nanocomposites (GHAp, CHAp), showing also a curvature for the initial period show, usually attributed to the boundary layer diffusion effects or external mass transfer effects [59]. In addition, the deviation of straight lines from the origin may be due to the difference in the rate of mass transfer in the initial and final stages of the adsorption [57].

3.2.4. Effect of initial dye concentration: isotherm analysis

To evaluate the maximum adsorption capacity of the adsorbents, the equilibrium adsorption of Rh 6G was studied as a function of variation in concentration (C_i = 5 to 75 mg L^{-1}) with a fixed amount of adsorbent dose (0.5 g L^{-1}). Langmuir and Freundlich isotherm models are used to describe the adsorption equilibrium data.

The Langmuir theory [60] is valid for monolayer adsorption onto a surface containing a finite number of identical sites, where no migration of the adsorbate in the plane of the surface is taking place and is expressed as:

$$q_e = \frac{q_m C_e K_L}{1 + K_L C_e} \tag{10}$$

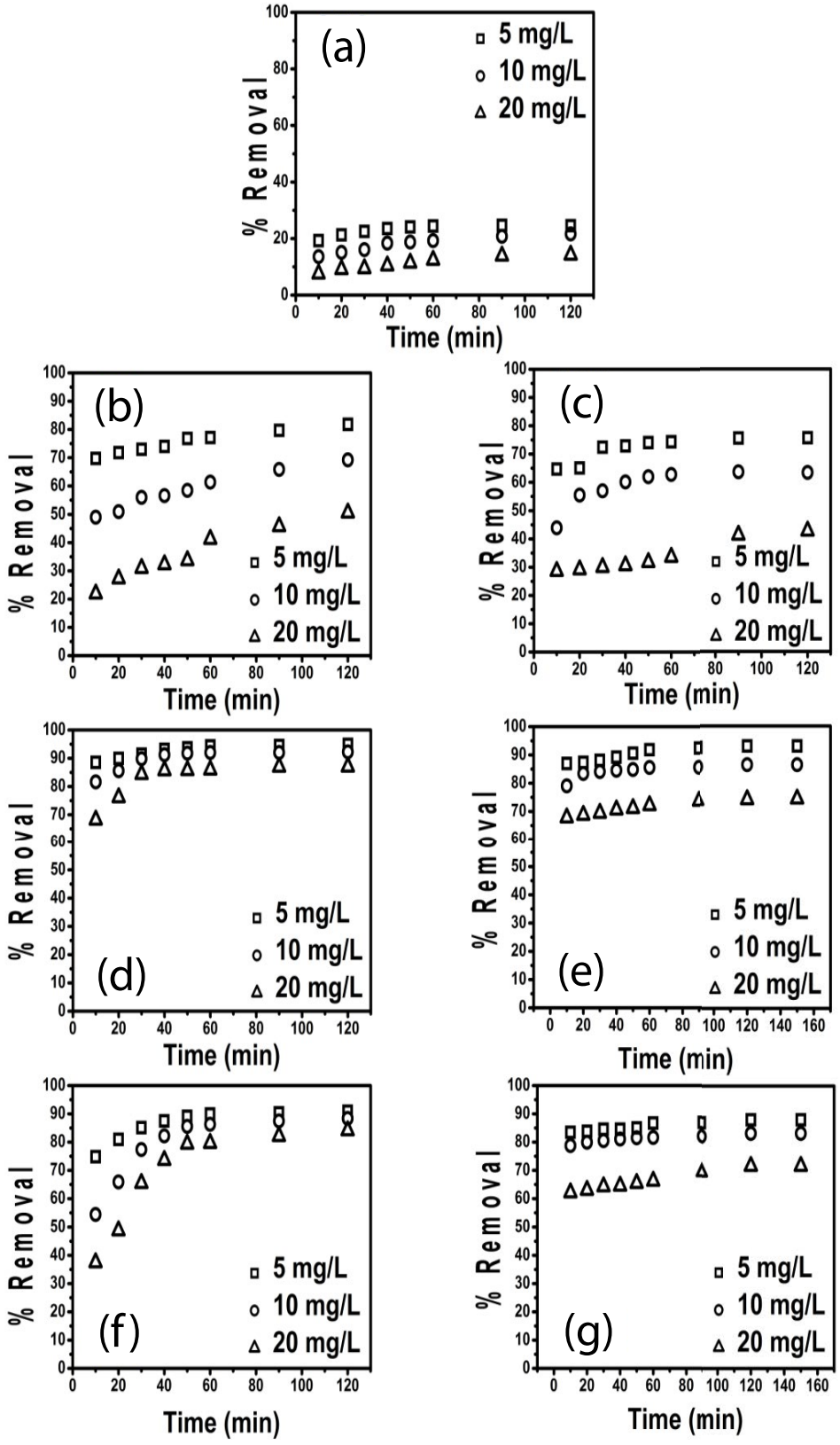

Fig. 8. Effect of contact time on Rh 6G dye adsorption by (a) HAp (synthesized), (b) Gra-C, (c) CNT-C, (d) GHAp 0.5, (e) GHAp 1, (f) CHAp 0.5, and (g) CHAp 1 adsorbent (initial Rh 6G dye concentrations – 5, 10, and 20 mg L^{-1}, adsorbent dose – 0.5 g L^{-1}).

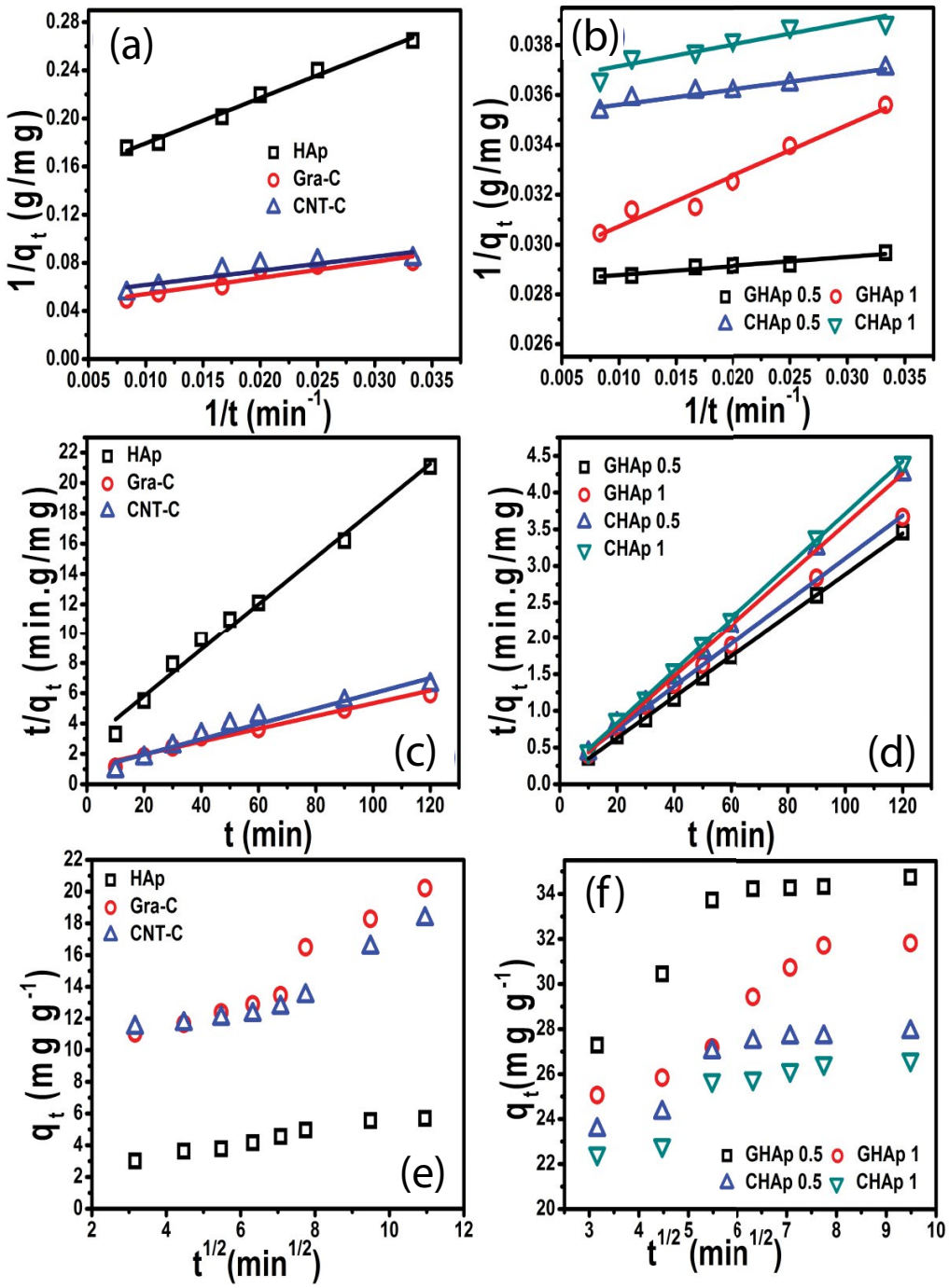

Fig. 9. Pseudo-first-order (a and b), pseudo-second-order (b and c) and intra-particle diffusion models (e and f) for Rh 6G dye adsorption (initial dye concentration of 20 mg L^{-1}, and adsorbent dosage of 0.5 g L^{-1}).

where q_e is the equilibrium concentration of the adsorbent (mg g^{-1}), q_m is the monolayer sorption capacity on the adsorbent (mg g^{-1}), and C_e is the equilibrium concentration in the solution (mg L^{-1}). The K_L is the Langmuir constant (L mg^{-1}), which is determined by plotting (C_e/q_e) vs. (C_e), representing the maximum adsorption capacity and energy constant linked to the heat of adsorption capacity. For fitting the experimental data, the Langmuir model is linearized as:

$$\frac{C_e}{q_e} = \frac{1}{q_m K_L} + \frac{C_e}{q_m} \tag{11}$$

As in being observed from the data collected in Table 3, the maximum monolayer coverage capacity (q_m) was 90.90 mg g^{-1} for GHAp 0.5, 76.33 mg g^{-1} for GHAp 1, 58.82 mg g^{-1} for CHAp 0.5, and 54.94 mg g^{-1} for CHAp 1, with an isotherm constant (K_L) of 0.29, 0.22, 0.25, and 0.23 L mg^{-1},

Table 2
Parameters of pseudo-first-order, pseudo-second-order and intra-particle diffusion kinetic models

Pseudo-first-order kinetic model					
Adsorbate	$q_{e(exp)}$ (mg g^{-1})	k_1 (min^{-1})	q_1 (mg g^{-1})	RMSE	R^2
HAp	5.69	26.58	7.057	0.55	0.98
Gra-C	20.22	33.02	24.63	1.80	0.86
CNT-C	18.28	23.47	20.04	0.71	0.78
GHAp 0.5	34.79	1.24	35.21	0.17	0.93
GHAp 1	32.83	7.05	34.84	0.82	0.95
CHAp 0.5	29.74	1.73	28.57	0.47	0.93
CHAp 1	26.65	2.29	26.64	0.044	0.85
Pseudo-second-order kinetic model					
Adsorbate	$q_{e(exp)}$ (mg g^{-1})	k_2 (min^{-1})	q_2 (mg g^{-1})	RMSE	R^2
HAp	5.69	0.0087	6.476	0.32	0.98
Gra-C	20.22	0.0015	23.80	1.46	0.96
CNT-C	18.28	0.00314	19.84	0.63	0.94
GHAp 0.5	34.79	0.011	35.71	0.37	0.99
GHAp 1	32.83	0.0052	34.24	0.57	0.99
CHAp 0.5	29.74	0.01351	28.90	0.34	0.99
CHAp 1	26.65	0.0110	27.93	0.52	0.99
Intra-particle-diffusion model					
Adsorbate	$q_{e(exp)}$ (mg g^{-1})	I (mg g^{-1})	K_p (mg g^{-1} min$^{-0.5}$)	RMSE	R^2
HAp	5.69	3.24	0.22	0.99	0.96
Gra-C	20.22	7.43	1.15	5.21	0.98
CNT-C	18.28	1.79	1.51	6.73	0.97
GHAp 0.5	34.79	33.13	0.16	0.68	0.88
GHAp 1	32.83	31.07	0.08	0.71	0.82
CHAp 0.5	29.74	26.68	0.12	1.24	0.91
CHAp 1	26.65	24.34	0.25	0.94	0.76

respectively, fitting quite well for all the adsorbents, as the values of R^2 were higher than 0.95. Comparably, the q_m was 6.45, 25, and 20 mg g^{-1} for HAp, Gra-C and CNT-C, respectively, indicating much improvement of active sites by HAp conjugation with Gra-C and CNT-C surfaces. The q_{max} for the removal of Rh 6G by GHAp and CHAp nanocomposites obtained from adsorption isotherms are quite good compared to previously reported adsorbents as listed in Table 4.

The Langmuir isotherm on the adsorption nature was further assessed by the following equation:

$$R_L = \frac{1}{1 + C_0 K_L} \tag{12}$$

where R_L is a dimensionless equilibrium parameter or the separation factor, and C_0 is the initial concentration of a metal solution (mg L^{-1}). The value of R_L denotes the adsorption nature to be unfavorable ($R_L > 1$), favorable ($0 < R_L < 1$), irreversible ($R_L = 0$), or linear ($R_L = 1$). According to Eq. (12), the values of R_L were found to be between 0.04–0.48 for different concentrations of Rh 6G, indicating that the adsorption process was favorable.

The Freundlich isotherm [60] model presumes that adsorption occurs on a heterogeneous surface through a multi-layer adsorption mechanism, and the adsorbed amount increases with the concentration leading to the following equation:

$$q_e = K_F C_e^{1/n} \tag{13}$$

which can be linearised by fitting the experimental data as follows:

$$\log q_e = \log K_F + \frac{1}{n} \log C_e \tag{14}$$

where q_e and C_e are adsorption at equilibrium concentrations (mg g^{-1}) on the adsorbent and in the liquid phase, while the constant K_F is an indicator of adsorption capacity (L mg^{-1}). The constant n is the empirical parameter related to the intensity of adsorption, which varies with the heterogeneity of the material. When $1/n$ values are in the range of $0.1 < 1/n < 1$, the adsorption process is favorable [61]. A smaller $1/n$ value indicates a more heterogeneous

Table 3
Parameters of the Langmuir isotherm model, separation factor (R_L) and Freundlich isotherm model

Langmuir isotherm model			
Adsorbate	q_m (mg g^{-1})	K_L (L mg^{-1})	R^2
HAp	6.45	0.21	0.98
Gra-C	25	0.38	0.98
CNT-C	20	0.45	0.99
GHAp 0.5	90.90	0.29	0.96
GHAp 1	76.33	0.22	0.97
CHAp 0.5	58.82	0.25	0.98
CHAp 1	54.94	0.23	0.98

Separation factor (R_L)							
Concentration	HAp	Gra-C	CNT-C	GHAp 0.5	GHAp 1	CHAp 0.5	CHAp 1
5	0.48	0.34	0.30	0.40	0.47	0.44	0.46
10	0.32	0.20	0.18	0.25	0.31	0.28	0.30
20	0.19	0.11	0.10	0.14	0.18	0.16	0.17
30	0.13	0.08	0.06	0.10	0.13	0.11	0.12
50	0.08	0.05	0.04	0.06	0.08	0.07	0.08

Freundlich isotherm model			
Adsorbate	K_f (mg g^{-1})	1/n	R^2
HAp	1.41	0.48	0.96
Gra-C	9.25	0.28	0.93
CNT-C	7.92	0.26	0.92
GHAp 0.5	19.95	0.53	0.99
GHAp 1	14.51	0.57	0.99
CHAp 0.5	13.32	0.45	0.98
CHAp 1	12.14	0.44	0.98

Table 4
Adsorbent materials with their adsorption capacity for Rh 6G dye

Sr. No.	Adsorbent	Experimental conditions	Adsorption capacity (mg g^{-1})	Ref.
1	Activated carbon	Dose – 1 g/100 ml, pH–7, contact time–48 h	44.7	[62]
2	Hexadecyl functionalized magnetic silica	pH – 10, contact time – 40 min	36.51	[63]
3	Graphene-oxide	Dose – 15 mgL^{-1}	23.3	[64]
4	Almond shell (*Prunus dulcis*)	Dose – 10 g L^{-1}, pH – 9, contact time – 500 min	32.6	[65]
5	Coffee – ground powder	pH – 2 contact time–3 h	17.37	[66]
6	Na^+-montmorillonite	Dose – 0.01/25 ml, contact time – 24 h	0.4	[67]
7	*Trichoderma harzianum* mycelial waste	Dose – 0.5 g L^{-1}, pH – 8, contact time – 140 min	3.40	[68]
8	Biological sludge	Dose – 1 g L^{-1}, pH – 7, contact time – 50 h	16.3	[69]
9	GHAp 0.5	Dose – 0.5 g L^{-1}, pH – 9, contact time – 300 min	90.90	This study
10	CHAp 0.5	Dose – 0.5 g L^{-1}, pH – 9, contact time – 300 min	58.82	This study

surface, whereas a value closer to or even 1 indicates the adsorbent has relatively more homogeneous binding sites. The parameters (Table 3) show that all composite adsorbents having R^2 values are close to 0.98–0.99, which indicates that the adsorption isotherms (Fig. 10) are fitted by the Freundlich equation to these samples as well. As $1/n < 1$, it indicates favorable and normal adsorption for all the samples. However, the $1/n$ of GHAp adsorbent samples are higher and closer to 1 than CHAp samples, indicating that GHAp adsorbents have relatively more homogeneous binding sites which is related to much lower of regularly distributed HAp particle on the Gra-C surfaces.

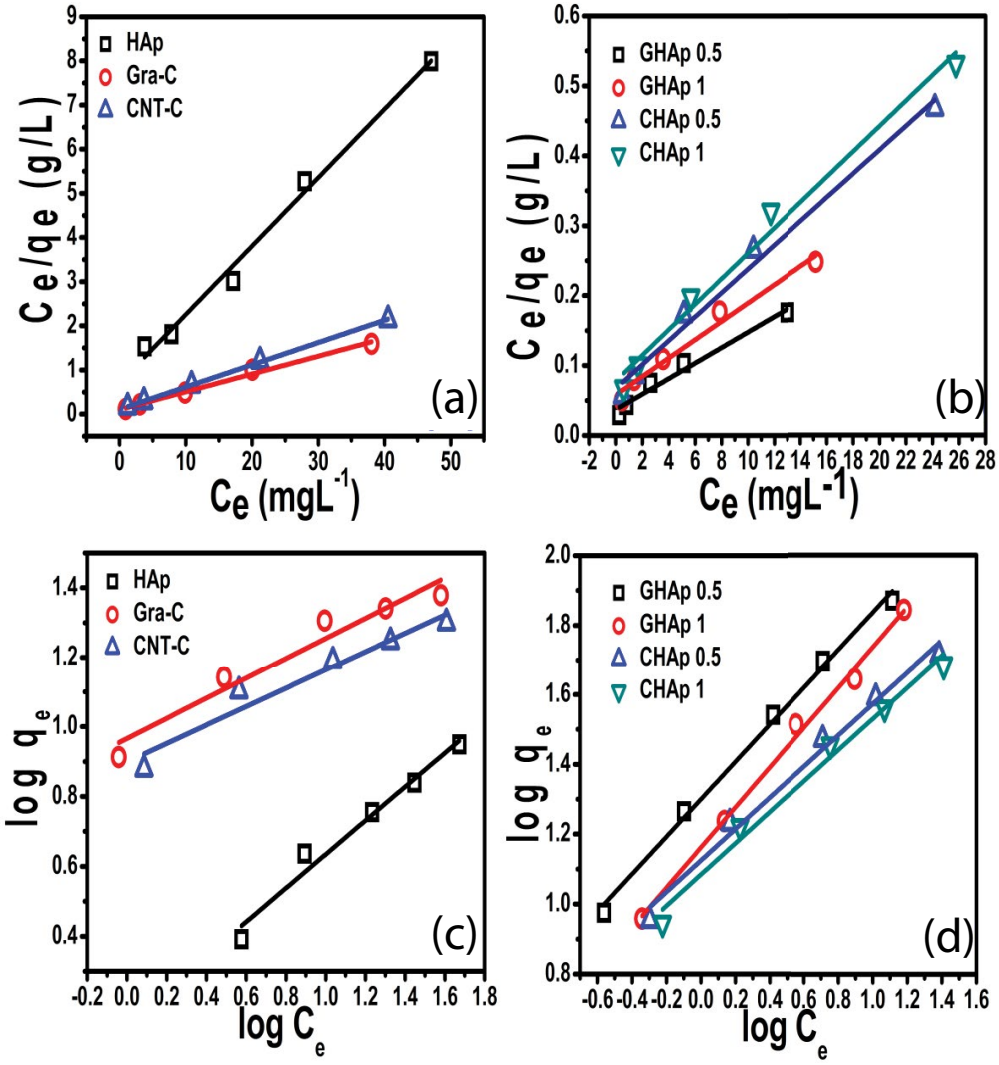

Fig. 10. Langmuir (a and b) and Freundlich (c and d) isotherms for Rh 6G dye adsorption (initial dye concentrations – 5 to 50 mg L^{-1}, adsorbent dose – 0.5 g L^{-1}).

3.3. Desorption and regeneration study

The adsorption performance of GHAp 0.5 and CHAp 0.5 in the reusability experiments was investigated, and the profile of three repeated experiments in the adsorption on Rh 6G is shown in Fig. 11. It can be seen that GHAp 0.5 and CHAp 0.5, have 77.24% and 69.39% of the adsorption efficiency respectively after three repeated cycles, proving GHAp 0.5 is an efficient adsorbent compared to the CHAp 0.5 nanocomposite.

4. Conclusion

The hydroxyapatite (HAp) is conjugated on carboxylated graphene nanoplatelets (GHAp) and multi-walled carbon nanotube (CHAp) surfaces, respectively, by its synthesis in-situ using chemical precursors and the wet precipitation process to increase the surface area and negatively-charged active sites for the removal of cationic Rh 6G dye from the aqueous solution. Spectroscopic, microscopic and zeta potential studies revealed the formation of GHAp and CHAp nanocomposites with more homogeneously located and smaller HAp particles on plane Gra-C, the crystalline structure, surface area and size of which is governed by the distribution of quantitatively higher carboxylic groups, being anchor sites for growing HAp. The dye removal is, thus, dependent primarily on the pH value, resulting in the surface ionic interactions of dye cations with available negative phosphate (from HAp) and remaining carboxylic (from Gra-C/CNT-C) groups, and, secondly, in the π–π electron donor-acceptor interaction between the C=C double bonds of dye benzene rings and nanomaterials. The adsorption data fitted better to the Freundlich than the Langmuir isotherm model, showing the maximum adsorption capacity for GHAp (90.90 mg g^{-1}), being followed by the monolayer adsorption capacity and heterogeneous sorption according to the pseudo-first- and pseudo-second-order kinetic models, respectively. The reusability of both GHAp and CHAp nanocomposites were also confirmed by 77.24% and 69.39% of adsorption efficiency, respectively, after three

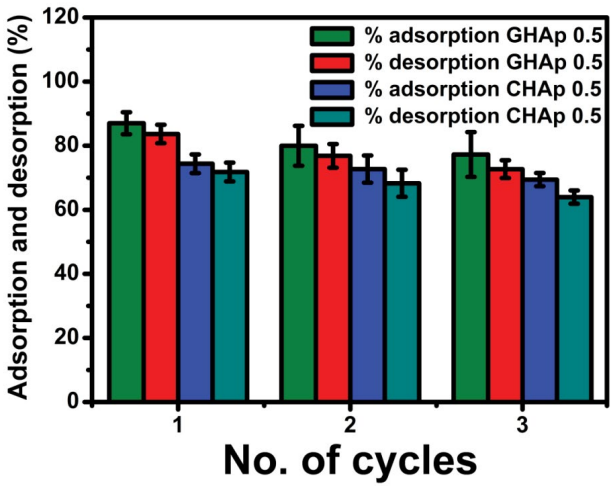

Fig. 11. Adsorption–desorption cycles of Rh 6G dye using GHAp and CHAp adsorbents of 0.5 g L^{-1} dose.

repeated cycles, showing their potential to be used as an efficient adsorbent with relatively high adsorption ability.

Acknowledgment

Authors are grateful to the Erasmus Mundus Project Euphrates (2013-2540/001-001-EMA2) for financial support.

References

[1] Y.C. Sharma, Optimization of parameters for adsorption of Methylene blue on a low-cost activated carbon, J. Chem. Eng. Data, 55 (2010) 435–439.
[2] R. Kant, Textile dyeing industry an environmental hazard, Nat. Sci., 4 (2012) 22–26.
[3] R.O.A. de Lima, A.P. Bazo, D.M.F. Salvadori, C.M. Rech, D. de Palma Oliveira, G. de Aragão Umbuzeiro, Mutagenic and carcinogenic potential of a textile azo dye processing plant effluent that impacts a drinking water source, Mutat. Res., 626 (2007) 53–60.
[4] R. Maas, S. Chaudhari, Adsorption and biological decolourization of azo dye Reactive red 2 in semicontinuous anaerobic reactors, Process Biochem., 40 (2005) 699–705.
[5] S. Kumar, S. Raut, P. Bandyopadhyay, Fungal decoloration and degradation of azo dyes: a review, Fungal Biol. Rev., 30 (2016) 112–133.
[6] T. Kim, C. Park, J. Yang, S. Kim, Comparison of disperse and reactive dye removals by chemical coagulation and Fenton oxidation, J. Hazard. Mater., 112 (2004) 95–103.
[7] D. Georgiou, P. Melidis, A. Aivasidis, K. Gimouhopoulos, Degradation of azo-reactive dyes by ultraviolet radiation in the presence of hydrogen peroxide, Dyes Pigm., 52 (2002) 69–78.
[8] S.S. Moghaddam, M.R.A. Moghaddam, M. Arami, Coagulation/flocculation process for dye removal using sludge from water treatment plant: optimization through response surface methodology, J. Hazard. Mater., 175 (2010) 651–657.
[9] S. Kuppusamy, K. Venkateswarlu, P. Thavamani, *Quercus robur* acorn peel as a novel coagulating adsorbent for cationic dye removal from aquatic ecosystems, Ecol. Eng., 101 (2017) 3–8.
[10] S. Raghu, C.A. Basha, Chemical or electrochemical techniques followed by ion exchange, for recycle of textile dye wastewater, J. Hazard. Mater., 149 (2007) 324–330.
[11] S. Karcher, A. Kornm, M. Jekel, Anion exchange resins for removal of reactive dyes from textile wastewaters, Water Res., 36 (2002) 4717–4724.
[12] L. Yang, Z. Wang, J. Zhang, Zeolite imidazolate framework hybrid nanofiltration (NF) membranes with enhanced permselectivity for dye removal, J. Membr. Sci., 532 (2017) 76–86.
[13] Y. Mansourpanah, M. Samimi, Preparation and characterization of a low-pressure efficient polyamide multi-layer membrane for water treatment and dye removal, Ind. Eng. Chem. Res., 53 (2017) 93–104.
[14] J. Abdi, M. Vossoughi, N. Mohammad, Synthesis of metal-organic framework hybrid nanocomposites based on GO and CNT with high adsorption capacity for dye removal, Chem. Eng. J., 326 (2017) 1145–1158.
[15] H. Zhu, R. Jiang, J. Li, Y. Fu, S. Jiang, J. Yao, Magnetically recyclable Fe_3O_4/Bi_2S_3 microspheres for effective removal of Congo red dye by simultaneous adsorption and photocatalytic regeneration, Sep. Sci. Technol., 179 (2017) 184–193.
[16] H.J. Kumari, P. Krishnamoorthy, T.K. Arumugam, S. Radhakrishnan, D. Vasudevan, An efficient removal of crystal violet dye from wastewater by adsorption onto TLAC/chitosan composite: a novel low-cost adsorbent, Int. J. Biol. Macromol., 96 (2017) 324–333.
[17] T.G. Chuah, A. Jumasiah, I. Azni, S. Katayon, S.Y.T. Choong, Rice husk as a potentially low-cost biosorbent for heavy metal and dye removal: an overview, Desalination, 175 (2005) 305–316.
[18] V. Vadivelan, K.V. Kumar, Equilibrium, kinetics, mechanism, and process design for the sorption of Methylene blue onto rice husk, J. Colloid Interface Sci., 286 (2005) 90–100.
[19] A. Saeed, M. Sharif, M. Iqbal, Application potential of grapefruit peel as dye sorbent: kinetics, equilibrium and mechanism of crystal violet adsorption, J. Hazard. Mater., 179 (2010) 564–572.
[20] R. Sivaraj, C. Namasivayam, K. Kadirvelu, Orange peel as an adsorbent in the removal of Acid violet 17 (acid dye) from aqueous solutions, Waste Manage., 21 (2001) 105–110.
[21] Y.B. Pottathara, VN. Narwade, K.A. Bogle, V. Kokol, TEMPO-oxidized cellulose nanofibrils–graphene oxide composite films with improved dye adsorption properties, Polym. Bull., 76 (2019) 1–15.
[22] S. Agarwal, I. Tyagi, V. Kumar, N. Ghasemi, Kinetics, equilibrium studies and thermodynamics of methylene blue adsorption on *Ephedra strobilacea* sawdust and modified using phosphoric acid and zinc chloride, J. Mol. Liq., 218 (2016) 208–218.
[23] V.S. Mane, P.V.V. Babu, Studies on the adsorption of Brilliant green dye from aqueous solution onto low-cost NaOH treated sawdust, Desalination, 273 (2011) 321–329.
[24] T. Maneerung, J. Liew, Y. Dai, S. Kawi, C. Chong, C. Wang, Activated carbon derived from carbon residue from biomass gasification and its application for dye adsorption: kinetics, isotherms and thermodynamic studies, Bioresour. Technol., 200 (2016) 350–359.
[25] V.O. Njoku, K.Y. Foo, M. Asif, B.H. Hameed, Preparation of activated carbons from rambutan (*Nephelium lappaceum*) peel by microwave-induced KOH activation for acid yellow 17 dye adsorption, Chem. Eng. J., 250 (2014) 198–204.
[26] U.I. A, G. Abdulraheem, S. Bala, S. Muhammad, M. Abdullahi, Kinetics, equilibrium and thermodynamics studies of C.I. Reactive blue 19 dye adsorption on coconut shell based activated carbon, Int. Biodeterior. Biodegrad., 102 (2015) 265–273.
[27] I. Khurana, A. Saxena, Removal of dyes using graphene-based composites: a review, Water Air Soil Pollut., 228 (2017) 180.
[28] V. Kumar, R. Kumar, A. Nayak, A. Saleh, M.A. Barakat, Adsorptive removal of dyes from aqueous solution onto carbon nanotubes: a review, Adv. Colloid Interface Sci., 194 (2013) 24–34.
[29] M.S. Mauter, M. Elimelech, Environmental applications of carbon-based nanomaterials, Environ. Sci. Technol., 42 (2008) 5843–5859.
[30] F. Perreault, A.F. De Faria, M. Elimelech, Environmental applications of graphene-based nanomaterials, Chem. Soc. Rev., 44 (2015) 5861–5896.
[31] P. Sharma, M.R. Das, Removal of a cationic dye from aqueous solution using graphene oxide nanosheets: investigation of adsorption parameters, J. Chem. Eng. Data, 58 (2013) 151–158.
[32] Y. Li, Q. Du, T. Liu, X. Peng, J. Wang, J. Sun, Y. Wang, S. Wu, Z. Wang, Y. Xia, L. Xia, Comparative study of Methylene blue

dye adsorption onto activated carbon, graphene oxide, and carbon nanotubes, Chem. Eng. Res. Des., 1 (2012) 361–368.
[33] C. Wu, Adsorption of reactive dye onto carbon nanotubes: equilibrium, kinetics and thermodynamics, J. Hazard. Mater., 144 (2007) 93–100.
[34] Y. Yao, F. Xu, M. Chen, Z. Xu, Z. Zhu, Adsorption behavior of Methylene blue on carbon nanotubes, Bioresour. Technol., 101 (2010) 3040–3046.
[35] C. Kuo, C. Wu, J. Wu, Adsorption of direct dyes from aqueous solutions by carbon nanotubes: determination of equilibrium, kinetics and thermodynamics parameters, J. Colloid Interface Sci., 327 (2008) 308–315.
[36] Y. Yao, S. Miao, S. Liu, L. Ping, H. Sun, S. Wang, Synthesis, characterization, and adsorption properties of magnetic Fe_3O_4 @graphene nanocomposite, Chem. Eng. J., 184 (2012) 326–332.
[37] L. Ai, C. Zhang, Z. Chen, Removal of Methylene blue from aqueous solution by a solvothermal-synthesized graphene/magnetite composite, J. Hazard. Mater., 192 (2011) 1515–1524.
[38] L. Fan, C. Luo, M. Sun, X. Li, F. Lu, H. Qiu, Preparation of novel magnetic chitosan/graphene oxide composite as effective adsorbents toward Methylene blue, Bioresour. Technol., 114 (2012) 703–706.
[39] H. Shi, W. Li, L. Zhong, C. Xu, Methylene blue adsorption from aqueous solution by magnetic cellulose/graphene oxide composite: equilibrium, kinetics, and thermodynamics, Ind. Eng. Chem. Res., 53 (2014) 1108–1118.
[40] VN. Narwade, S.R. Anjum, V. Kokol, R.S. Khairnar, Ammonia-sensing ability of differently structured hydroxyapatite blended cellulose nanofibril composite films, Cellulose, 26 (2019) 3325–3337.
[41] A. Corami, S. Mignardi, V. Ferrini, Copper and zinc decontamination from single- and binary-metal solutions using hydroxyapatite, J. Hazard. Mater., 146 (2007) 164–170.
[42] V.N. Narwade, R.S. Khairnar, V. Kokol, In-situ synthesized hydroxyapatite–cellulose nanofibrils as biosorbents for heavy metal ions removal, J. Polym. Environ., 26 (2017) 2130–2141.
[43] A. Corami, S. Mignardi, V. Ferrini, Cadmium removal from single- and multi-metal (Cd + Pb + Zn + Cu) solutions by sorption on hydroxyapatite, J. Colloid Interface Sci., 317 (2008) 402–408.
[44] T.K. Mahto, S.C. Pandey, S. Chandra, A. Kumar, Hydroxyapatite conjugated graphene oxide nanocomposite: a new sight for significant applications in adsorption, RSC Adv., 5 (2015) 96313–96322.
[45] C. Srilakshmi, R. Saraf, Ag-doped hydroxyapatite as efficient adsorbent for removal of Congo red dye from aqueous solution: synthesis, kinetic and equilibrium adsorption isotherm analysis, Microporous Mesoporous Mater., 219 (2016) 134–144.
[46] V.N. Narwade, R.S. Khairnar, Cobalt adsorption on the nano-hydroxyapatite matrix: isotherm and kinetic studies, Bull. Pol. Acad. Sci. Tech. Sci., 65 (2017) 131–137.
[47] V.N. Narwade, R.S. Khairnar, V. Kokol, In-situ synthesized hydroxyapatite-loaded films based on cellulose nanofibrils for phenol removal from wastewater, Cellulose, 24 (2017) 4911–4925.
[48] S. Sasi, A. Murali, S.V. Nair, A.S. Nair, K.R.V. Subramanian, The effect of graphene on the performance of an electro-chemical flow capacitor, J. Mater. Chem. A, 3 (2015) 2717–2725.
[49] S.K. Mishra, S.N. Tripathi, V. Choudhary, B.D. Gupta, Surface plasmon resonance-based fiber optic methane gas sensor utilizing graphene-carbon nanotubes-poly(methyl methacrylate) hybrid nanocomposite, Plasmonics, 10 (2015) 1147–1157.
[50] S. Taha, S. Begum, V.N. Narwade, D.I. Halge, J.W. Dadge, M.P. Mahabole, R.S. Khairnar, K.A. Bogle, Development of alcohol sensor using TiO_2-hydroxyapatite nano-composites, Mater. Chem. Phys., 240 (2020) 122228.
[51] S.R. Anjum, V.N. Narwade, K.A. Bogle, R.S. Khairnar, Graphite doped hydroxyapatite nanoceramic: selective alcohol sensor, Nano-Struct. Nano-Objects, 14 (2018) 98–105.
[52] Z.H. Cheng, A. Yasukawa, K. Kandori, T. Ishikawa, FTIR study on incorporation of CO into calcium hydroxyapatite, J. Chem. Soc., Faraday Trans., 94 (1998) 1501–1505.
[53] Z.H. Cheng, A. Yasukawa, K. Kandori, T. Ishikawa, FTIR study of adsorption of CO_2 on nonstoichiometric calcium hydroxyapatite, Langmuir, 14 (1998) 6681–6686.
[54] A. Janković, S. Eraković, M. Mitrić, I.Z. Matić, Z.D. Juranić, G.C.P. Tsui, C.Y. Tang, V. Mišković-Stanković, K.Y. Rhee, S.J. Park, Bioactive hydroxyapatite/graphene composite coating and its corrosion stability in simulated body fluid, J. Alloys Compd., 624 (2015) 148–157.
[55] M.F. Cipreste, I. Gonzalez, A.M. Goes, W. Augusto, D.A. Macedo, Attaching folic acid on hydroxyapatite nanorod surfaces: an investigation of the HA – FA interaction, RSC Adv., 6 (2016) 76390–76400.
[56] H. Bouyarmane, S. El Asri, A. Rami, C. Roux, M.A. Mahly, A. Saoiabi, T. Coradin, A. Laghzizil, Pyridine and phenol removal using natural and synthetic apatites as low-cost sorbents: influence of porosity and surface interactions, J. Hazard. Mater., 181 (2010) 736–741.
[57] C. Santhosh, E. Daneshvar, P. Kollu, S. Peräniemi, A. Nirmala, A. Bhatnagar, Magnetic SiO_2@$CoFe_2O_4$ nanoparticles decorated on graphene oxide as efficient adsorbents for the removal of anionic pollutants from water, Chem. Eng. J., 322 (2017) 472–487.
[58] V. Fierro, V. Torné-Fernández, D. Montané, A. Celzard, Adsorption of phenol onto activated carbons having different textural and surface properties, Microporous Mesoporous Mater., 111 (2008) 276–284.
[59] H. Asfour, O. Fadali, Equilibrium studies on adsorption of basic dyes on hardwood, J. Chem. Technol. Biotechnol., 35 (1985) 21–27.
[60] K.Y. Foo, B.H. Hameed, Insights into the modeling of adsorption isotherm systems, Chem. Eng. J., 156 (2010) 2–10.
[61] A.H. Gedam, R.S. Dongre, Adsorption characterization of Pb(II) ions onto iodate doped chitosan composite: equilibrium and kinetic studies, RSC Adv., 5 (2015) 54188–54201.
[62] G. Annadurai, R. Juang, D. Lee, Adsorption of Rhodamine 6G from aqueous solutions on activated carbon, J. Environ. Sci. Health., Part A, 36 (2001) 715–725.
[63] Y. Chang, C. Ren, Q. Yang, Z. Zhang, L. Dong, X. Chen, Preparation and characterization of hexadecyl functionalized magnetic silica nanoparticles and its application in Rhodamine 6G removal, Appl. Sci. Res., 257 (2011) 8610–8616.
[64] H. Ren, D.D. Kulkarni, R. Kodiyath, W. Xu, I. Choi, Competitive adsorption of dopamine and Rhodamine 6G on the surface of graphene oxide, ACS Appl. Mater. Interfaces, *6* (2014) 2459–2470.
[65] H.B. Senturk, D. Ozdes, C. Duran, Biosorption of Rhodamine 6G from aqueous solutions onto almond shell (*Prunus dulcis*) as a low-cost biosorbent, Desalination, 252 (2010) 81–87.
[66] K. Shen, M.A. Gondal, Removal of hazardous Rhodamine dye from water by adsorption onto exhausted coffee ground, J. Saudi Chem. Soc., 21 (2017) S120–S127.
[67] A.H. Gemeay, Adsorption characteristics and the kinetics of the cation exchange of Rhodamine-6G with Na + -Montmorillonite, J. Colloid Interface Sci., 241 (2002) 235–241.
[68] S.Ã. Sadhasivam, S. Savitha, K. Swaminathan, Exploitation of *Trichoderma harzianum* mycelial waste for the removal of Rhodamine 6G from aqueous solution, J. Environ. Manage., 85 (2007) 155–161.
[69] G. Annadurai, R.S. Juang, P.S. Yen, D.J. Lee, Use of thermally treated waste biological sludge as dye absorbent, Adv. Environ. Res., 7 (2003) 739–744.